Formation of graphene and hexagonal boron nitride on Rh(111) studied by in-situ scanning tunneling microscopy

Dong, G.

Cover Page

Universiteit Leiden

Leiden University Repository

The handle http://hdl.handle.net/1887/20105 holds various files of this Leiden University dissertation.

Author: Dong, Guocai
Title: Formation of graphene and hexagonal boron nitride on Rh(111) studied by in-situ scanning tunneling microscopy
Date: 2012-11-07

Chapter 2 Experimental

2.1 Experimental setup

2.1.1 Vacuum chamber and equipment

All measurements in this thesis were performed with a dedicated STM-setup in the Kamerlingh Onnes Laboratory of Leiden University. This setup consisted of a single ultrahigh vacuum (UHV) chamber, equipped with a scanning tunneling microscope (STM), a low-energy electron diffraction (LEED) apparatus, an Auger electron spectroscopy (AES) instrument, and a quadrupole mass spectrometer (QMS), for analysis purposes[1].

The base pressure of the vacuum system was 1.5 x 10^{-11} mbar. During measurements, the vacuum level was kept below 2 x 10^{-10} mbar. To achieve and maintain this vacuum, a single 170 liter/second magnetically levitated turbo-molecular pump, a 410 liter/second ion getter pump, and a titanium sublimation pump, integrated into a cold trap, were connected to the UHV chamber. Also, the entire vacuum system was extensively degassed by a bake-out procedure up to 450 K and the sample holder and STM components were further degassed by prolonged annealing of the Rh sample to 800K.

The pressure in the UHV system was measured by an ion gauge in the middle of the chamber. The measured pressure had not been corrected for the different sensitivities to

---

[1] Instruments and techniques that are considered standard for surface science will not be given a detailed introduction in this thesis. The operation principles of these can be found in most surface science textbooks.

different gases. The difference in location of the pressure gauge and the sample may have resulted in a further error in the recorded pressure. To correct for these errors, a calibration experiment using borazine deposition (section 5.3) was performed, and the calibration constant for ethylene was calculated from that for borazine, using the known relative sensitivities for the two gases.

To reduce the effect of vibrations on the STM measurements, several isolation stages were combined. The entire setup rested on four air legs, which were placed on a foundation separated from the foundation of the building. The setup was thus effectively decoupled from the vibrations of the building. The rotation pump that was connected to the turbo-molecular pump was placed on the building foundation, and its connection to the turbo-pump was made by long, flexible bellows. In this way, the effect of vibrations from the rotation pump was also reduced to a minimum. The influence of the vibrations of the turbo-pump was minimized by connecting it to the UHV chamber via bellows with a damping jacket. Together with the magnetic bearings of the turbo-pump, these measures reduced the residual vibrations in the STM images to such a low level that atomic resolution could be achieved even with the turbo-pump and the rotation pump running.

The rhodium sample was cleaned routinely by Ar^+ ion bombardment and annealing. The Ar^+ ions were produced in a differentially pumped, focused ion gun, fitted with a Wien mass filter. With the differential pumping on the ionization chamber, the pressure in the main chamber did not exceed 1×10^{-8} mbar, while the pressure in the ionization chamber was held at 5×10^{-4} mbar. The focusing and alignment of the ion beam were optimized with the help of a dummy sample in the form of a Faraday cup. The diameter of the beam was less than 1 mm, which is smaller than the size of the sample, so a 5×5 mm^2 scanning was applied by use of sweep voltages on the deflection plates of the ion gun, in order to clean the whole sample. The sample holder was made of molybdenum, and coated by the sample material, in this case Rh, to avoid sputter deposition on the sample of other materials from the sample holder.

High-purity borazine (HBNH)$_3$, was synthesized by the research group of Prof. Hermann Sachdev (University of Saarland). It was dosed into the UHV-system via a dosing valve from a container in which the material was stored at a reduced temperature, by means of a Peltier cooler. The container and dosing system were obtained from the research group of Prof. Jürg Osterwalder and Prof. Thomas Greber (University of Zurich). For each deposition experiment, the borazine was allowed to warm up temporarily. Ethylene
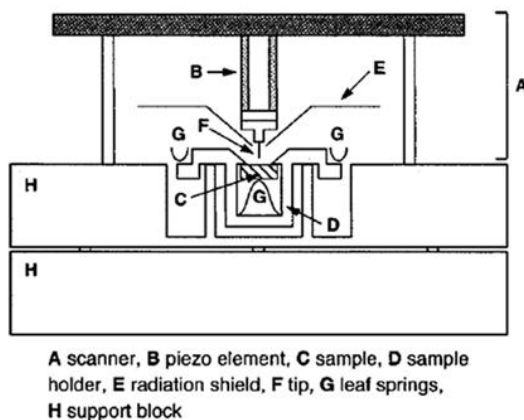
gas with a purity of 99.99% was purchased from ALDRICH^{TM}. This gas was dosed through a leak valve. The connections between gas bottles and valves were 6 mm stainless steel pipes. A turbo-pump was used to evacuate these gas lines. For high-purity deposition results it proved to be important to keep these lines clean by degassing (heating) and flushing them with the gas of choice (borazine or ethylene).

2.1.2   The Variable-Temperature STM

The central part of the setup was an STM, which had been optimized for (fast) scanning at high sample temperatures and also during substantial temperature variations [33, 34]. Like most other STMs, our Variable-Temperature STM (VT-STM) is using a piezoelectric tube, in our case with a length of 12 mm, to scan regions up to typically 3 x 3 μm^2, with sub-nanometer resolution. The macroscopic dimensions of the piezo element, the sample and other components in the mechanical path between the tip and the sample make that even modest temperature variations can cause a significant drift in an STM image. More dramatically, when the component of this drift in the z-direction, along the tip axis, were to exceed the control range of the piezo element, this would lead either to a situation where the surface drifts out of range or to a crash of the tip into the sample surface. For these reasons, most STMs are used either at room temperature or at a constant, low or (modestly) elevated temperature, at which the sample and microscope are first allowed to equilibrate for a long time, typically several hours, prior to the coarse tip-sample approach and imaging. The STM we were using could compensate for thermal drifts in all directions by its special design. The details of this can be found in ref [33]. Here, only a brief summary is given. As shown in Fig. 2.1, in the scanner, a radiation shield protects the piezo element from thermal radiation from the sample. Apart from its three legs, the scanner is cylindrically symmetrical around the axis of the tip. A finite-element analysis of the scanner was utilized to match the expansion of the legs with that of the assembly of the piezo element, the tip holder and the tip, in order to minimize the vertical drift of the tip, due to temperature changes of these components of the microscope. The sample was clamped into a molybdenum holder, with its surface against two ledges. The holder itself was clamped down with two extending arms on two supports. The ledges, the arms, and the supports all reside in the same plane, coinciding with the precise level of the tip apex. This configuration ensured that also expansions of the sample and its holder did not affect the vertical position of the surface plane with

respect to the tip. With this design, neither the expansion of the piezo element and other components of the microscope nor that of the sample and sample holder can give rise to a significant tip-sample distance variation. In practice, experiments have been performed without the need for any mechanical adjustments in the tip height, while the sample temperature was being changed from 300 K to approximately 1200 K. In section 9.2, an example is given in which the same area of the sample was followed by the STM during a 50°C temperature variation.

A scanner, **B** piezo element, **C** sample, **D** sample holder, **E** radiation shield, **F** tip, **G** leaf springs, **H** support block

Fig. 2.1 Schematic cross section of the STM. The scanner A is cylindrically symmetric around the axis through the tip F. It rests with three legs on the support block H. A radiation shield E protects the piezo element B against thermal radiation from the sample C. The sample holder D is clamped down against two supports by leaf springs G. The sample is clamped up against two ledges of the sample holder. (from ref [33])

Fig. 2.2 (a) shows a schematic top view of the holder. Four arms extend from the holder. Two of these are rotated against vertical posts, which form part of the Mo support block. The other two are shaped like knife-edges and are pressed down against two oppositely tilted supports by two leaf springs. When the holder is heated, it expands outwards along the four extensions, but the center stays at its original position. To make coarse adjustment possible, the tip is mounted 1 mm outside this stable center position. When the sample holder is placed in the support block, it first makes contact with the vertical posts. At that stage, the sample holder still has the freedom to rotate around the axis through these first two contact points. This rotational freedom ensures that both knife-

edges will make contact with their supports, when the holder is pushed further into its final position. In this way, a completely unstrained four-point mechanical contact is established. Once in place, the sample holder can still rotate around the two knife-edges, which allows coarse adjustment of the tip-sample separation. This design, together with the choice of low-expansion-coefficient materials, makes it possible to follow the same area on the surface during hundreds of degrees of temperature variation.

A post, B arm, C leaf spring, D stable center,
E knife edge, F rotation axis
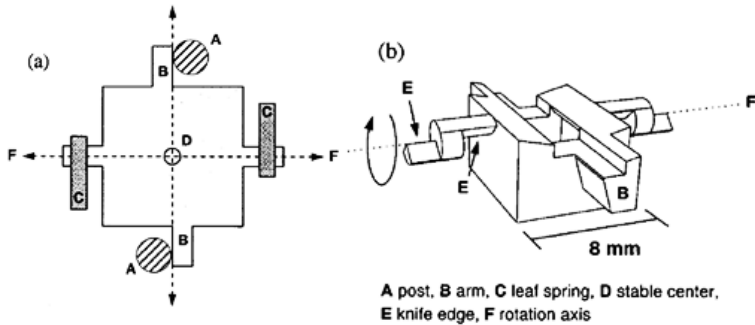
Fig. 2.2 Schematic top view of the sample holder body. The center circle D denotes the point from which all the lateral expansions are directed outwards. (b) A perspective drawing of the sample holder. The sample holder can rotate around the axis F, defined by the knife edges E. (from ref. [33])

In addition to the drift-minimizing mechanical design, the STM electronics have been optimized to scan fast. It has been demonstrated that the STM can image surfaces at video rate (24 frames per second) [34] (A commercial version of this instrument is marketed by Leiden Probe Microscopy BV, www.leidenprobemicroscopy.com). Because of the critical experimental conditions, in particular the high temperatures during deposition, video-rate scanning is very difficult. Therefore, the high-speed capabilities of the VT-STM have not been exploited directly in the work described in this thesis. On the other hand, the low noise level that the high-speed electronics has at low frequencies and the modular design of the electronics provided stable scanning conditions plus possibilities for customization of the scans, which played an important role in this work.

2.1.3   The heating of the sample

There were several requirements on the heating system of the sample. The experiments in this thesis required stable elevated sample temperatures up to 1200 K. The cleaning of the Rh sample required a maximum temperature of 1300 K. The surroundings should be kept at a relatively low temperature in order to maintain a low degassing rate and, thus, a low rate of contamination on the sample. Finally, the lifetime of the heating system needed to be long, in order to enable routine, long-duration experiments at high temperature.

A sketch of the sample heating system is shown in Fig. 2.3. We chose to use a tungsten filament with which we could heat the sample both by thermal radiation and by electron bombardment. The heating efficiency was optimized by a quartz tube (part C) that was placed around the filament. The quartz tube reduced the thermal radiation from the filament to the sample holder, so that the sample holder remained colder while the sample was hot. Sublimation of tungsten from the filament led to a conductive coating on the inner side of the tube, which was not connected conductively to the sample or the metallic components of the sample holder. Therefore, during electron bombardment, when the filament was biased to a high, negative voltage of typically -600 V, while the sample was held at ground potential, the metal film in the tube charged up negatively. This made the tube act as a lens, focusing the electrons that were emitted by the filament, onto the sample, which improved the heating efficiency of the sample, while reducing the heat load on the holder. During the mounting of the sample holder, the transparent quartz tube made it easier to place the filament as close as possible to the sample, which also increased the efficiency of the thermal radiation heating. A small tantalum spring (part F) was positioned between the quartz tube and the sample, to accommodate the thermal expansion difference between the tube and the Mo sample holder. The inner scale of the spring was larger than the inner diameter of the tube, so that the metal deposited from the filament would not make a short circuit between the filament and the sample. For the same purpose, a ceramic part E was used to hold the tube and the sample, and provided insulation between the filament and the parts at ground potential. Using this sample holder, the sample could be heated from room temperature to 1300 K in 10 seconds. Experiments in which the sample was held at 1000 K or higher for hours, while the background pressure in the UHV chamber stayed below 5 x 10^{-10} mbar, became a routine.
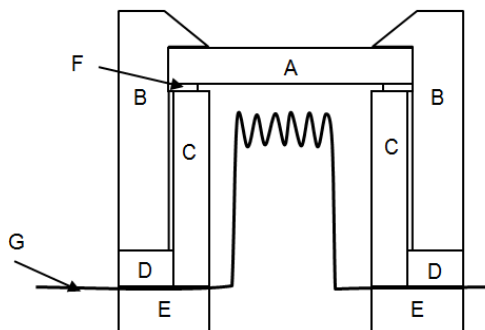
Fig. 2.3 A sketch of the heating system for the sample. A sample; B Mo sample holder; C quartz tube; D insulating ceramic parts; E a larger ceramic part which holds the quartz tube; F springs to accommodate the thermal expansion difference between C and B; G filament.

In our experiments it proved to be of crucial importance that the measurement of the sample temperature was accurate (within 5 K) and reproducible (within 1 K). For example, it was by virtue of our reliable temperature scale that we could identify the narrow temperature window of about 40°C in section 8.2, in which graphene is formed and carbide is not. In Chapter 6, the disappearance temperature of the nanomesh overlayer was determined twice, in two separate experiments, in both cases resulting in precisely the same temperature of 1160 K. In practice, we found that accurate measurements of the sample temperature were not straightforward. For example, when the Rh sample was heated to 1000 K, even the part of the Mo sample holder that was directly touching the sample, responded with a significant time delay and when it reached its final temperature it was still approximately 300 K colder than the sample. We paid specific attention to four aspects to achieve the required quality of the temperature measurement. First of all, the temperature measurement was performed by use of a K-type thermocouple directly on the Rh sample. Secondly, in order to avoid a temperature difference between the sample and the junction of the thermocouple, the two wires of the thermocouple were connected separately to the Rh, each onto one of the edges of the sample. Third, in order to make sure that the ends of the thermocouple wires were really at the temperature of the sample, the connections were made by spot welding, which was performed by use of a laser spot welding machine. Finally, the pins and sockets,

used for connecting the thermocouple wires between the sample holder and the support block and the wires running between the sockets on the support block and the feedthroughs on the UHV chamber were all made out of the appropriate K-type thermocouple materials, in order to properly define the reference temperature with respect to which the thermovoltage was measured, irrespective of the slowly drifting temperature of the passively heated support block.

2.2 The Rh(111) sample

A clean Rh sample formed the essential starting point for well-defined experiments, as presented in this thesis, for both the projects of graphene growth and of nanomesh growth. Because most of the experiments required elevated temperatures, where rapid diffusion can make near-surface contaminants segregate to the surface, the Rh sample should not only be clean at room temperature, but had to stay clean even at elevated temperatures, throughout the entire experiment.

The Rh single crystal was purchased from Surface Preparation Laboratory[TM], where it had been aligned by use of Laue diffraction to within 0.1 degree of the (111) orientation, spark eroded to dimensions of 4.8 x 4.8 x 1 mm^3, and mechanically polished. In the UHV chamber, the (111) surface of the Rh sample was cleaned by cycles of Ar$^+$ ion sputtering, followed by flash annealing to 1300 K. Then the sample was exposed to 2 - 3 $\times 10^{-7}$ mbar O_2 for 1 to 2 hours, at a temperature of 700 to 800 K; this latter step proved necessary, for removal of carbon surface contamination, defusing from the bulk. Residual O was removed from the Rh surface by flashing the sample to 1000 K [73]. The Ar$^+$ sputtering was performed with the focused sputter gun (see section 2.1.1), at a current of 280 nA and a energy of 800 eV, for 30 to 45 minutes. Although cycles of sputtering and annealing can remove most of the contaminants in the near-surface region of the sample, the total amount of carbon in the sample is hardly changed. Delouise et.al. already reported that the carbon remnants in Rh can form a graphite structure during annealing, and that this graphite can then be reacted away by oxygen at elevated temperatures [73]. This process has been followed by STM (one example can be found in Chapter 12.). When the surface of Rh was fully covered by graphene, the oxidation reaction of the carbon was very slow. If there were uncovered Rh areas, the reaction took place at the

edges of the graphene, with a very noticeable speed. When the surface was fully covered by graphene or by graphite, Ar$^+$ ion bombardment introduced defects in the overlayer, from which the oxidation reaction could proceed. As shown in Chapter 13, we also learned that the elevated temperature was necessary for carbon diffusion from the bulk to the surface. When the concentration of carbon adatoms on the Rh surface exceeded a critical value, graphene or carbide islands could form on the surface. After nucleation of such islands, carbon atoms that segregated from the bulk to the surface contributed only to further growth of these islands. This process decreased the carbon concentration in the bulk material. This is also why annealing at 1300 K was necessary, before oxygen treatment, to make dissolved carbon atoms segregate to the surface and become incorporated in graphene or another carbon-containing surface species, where they could be removed by oxidation. In the beginning of the cleaning process, even brief annealing at 1000 K was sufficient to bring one layer of carbon to the surface, as indicated by AES. After tens of cleaning cycles, the quality of the sample was checked by LEED, AES, and more importantly, by STM. Although STM does not have elemental resolution, a clean STM image, without local protrusions or depressions and without pinning or decoration of the steps, provided very strong evidence for the cleanness of the sample. Furthermore, we tested the sample during heating up to the experimental temperature, for times that were comparable to those that were needed for one measurement. This provided the experiments in this thesis with a very well-defined substrate.

2.3   The moiré patterns

Because of lattice mismatch between graphene or *h*-BN and Rh(111), moiré patterns appeared in the STM images of *h*-BN and graphene. The moiré pattern behavior could be used as a magnifier of lattice defects, allowing us to get atomic information, even without always actually having atomic resolution. Obtaining atomic resolution with an STM is a serious challenge at high temperatures, which makes moiré patterns a very useful tool. To translate the moiré pattern to an atomic model, one of the easiest ways is go to reciprocal space [74]. The moiré pattern resulting from the combination of two hexagonal lattices, with different periods and different orientations, is also a hexagonal lattice. If $\vec{k}_1$ and $\vec{k}_2$ both designate one of the principal reciprocal lattice vectors of the

two hexagonal lattices, we can immediately obtain one of the principal reciprocal lattice vectors $\vec{k}_m$ of the moiré pattern as their difference

$$\vec{k}_m = \vec{k}_1 - \vec{k}_2 \; .$$ Eq. 2.1

With this, one can easily calculate that the apparent rotation angle α between the moiré pattern and the Rh(111) lattice and the actual rotation angle β between the lattice of the *h*-BN or graphene overlayer and the Rh(111) substrate are related via

$$\sin \alpha = \frac{d_1 \sin \beta}{\sqrt{d_1^{\,2} + d_2^{\,2} - 2d_1 d_2 \cos \beta}}$$; Eq. 2.2

d_1 is the lattice constant of the overlayer and d_2 is the lattice constant of the Rh(111) substrate. The moiré pattern lattice constant (d_m) is

$$d_m = \frac{d_1 d_2}{\sqrt{d_1^{\,2} + d_2^{\,2} - 2d_1 d_2 \cos \beta}}$$. Eq. 2.3

Note here the moire lattice does not necessarily corresponds to a rational fit between the two lattices. In most cases, the lattices do not precisely coincide at regular distances. Only for special ratios between lattice constants and for special angles will the combined 2-lattice system be really periodic with the periodicity of the moire lattice. However, the calculated d_m and α still represents a beating pattern between the two lattice, which can still be measured by for example STM.

Due to the six-fold symmetry of *h*-BN and graphene, the geometry of the overlayer and the moiré pattern is the same when the rotation angle β of the overlayer is changed by integer multiples of 60°. In our calculations we therefore restricted the range of β to the interval between -30° and 30°. Due to the symmetry of the substrate there is an intrinsic *n* x 60° ambiguity in the principal lattice direction of the substrate with respect to which the moiré pattern rotation has to be specified. As a result of this, we also present the calculated moiré pattern orientation angles α in the interval between -30° and 30°. The calculated relations between the rotation angle β of the overlayer and the orientation α (Eq. 2.2) and lattice constant d_m (Eq. 2.3) of the moiré pattern are shown for *h*-BN and graphene in Fig. 2.4 and Fig. 2.5, respectively.
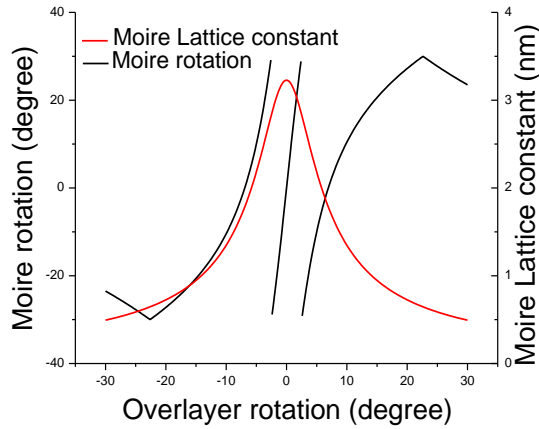
Fig. 2.4 Relation calculated between the overlayer rotation angle β and the orientation angle α (black curve) and lattice constant d_m (red curve) of the moiré pattern for *h*-BN on Rh (111).
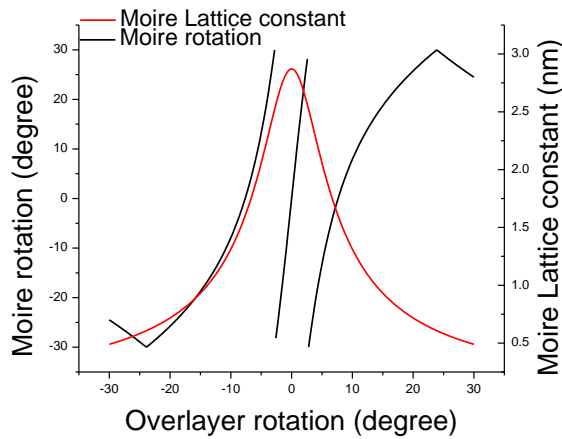
Fig. 2.5 Relation calculated between the overlayer rotation angle β and the orientation angle α (black curve) and lattice constant d_m (red curve) of the moiré pattern for graphene on Rh (111).

The two figures show that the rotation of the overlayer is amplified very much by the moiré pattern, but that the mere measurement of the rotation angle α of a moiré pattern is not enough to derive the rotation angle *β* of the overlayer.

Moiré patterns also amplify translational errors of the overlayer. If a patch of graphene or *h*-BN is translated over a distance $\vec{S}$ with respect to the original position, the accompanying displacement of the moiré pattern $\vec{M}$ is:

$$\overrightarrow{M} = -\frac{L_m}{L_O}\,\vec{S}$$

Eq. 2.4

.

Here, L_m and L_o are the periodicities in the $\vec{S}$ direction for the moiré pattern and the overlayer, respectively. Because L_m is larger than L_o, transitional errors are amplified by the moiré patterns by a factor of $L_m/L_o > 1$.